

Targeted insult to subsurface cortical blood vessels using ultrashort laser pulses: three models of stroke

Nozomi Nishimura^{1,2}, Chris B Schaffer^{1,2}, Beth Friedman³, Philbert S Tsai^{1,2}, Patrick D Lyden^{3,4} & David Kleinfeld^{1,2,4}

We present a method to produce vascular disruptions within rat brain parenchyma that targets single microvessels. We used two-photon microscopy to image vascular architecture, to select a vessel for injury and to measure blood-flow dynamics. We irradiated the vessel with high-fluence, ultrashort laser pulses and achieved three forms of vascular insult. (i) Vessel rupture was induced at the highest optical energies; this provides a model for hemorrhage. (ii) Extravasation of blood components was induced near the lowest energies and was accompanied by maintained flow in the target vessel. (iii) An intravascular clot evolved when an extravasated vessel was further irradiated. Such clots dramatically impaired blood flow in downstream vessels, in which speeds dropped to as low as ~10% of baseline values. This demonstrates that a single blockage to a microvessel can lead to local cortical ischemia. Lastly, we show that hemodilution leads to a restoration of flow in secondary downstream vessels.

Brain homeostasis depends on adequate levels of blood flow to ensure the delivery of nutrients to brain cells, and to facilitate the removal of metabolites and heat. In the cerebral cortex, the vasculature forms networks of subsurface microvessels. In principle, these networks provide several routes for blood to flow to the same cortical column^{1–4}. Notably, these microvessels are an important locus of cerebral vascular disease, as their dysfunction contributes to cognitive impairment in disorders such as vascular dementia, Alzheimer disease and ‘silent’ stroke^{5–7}. But the development of models of microvessel dysfunction has been problematic as it has been difficult to selectively target and lesion cerebral microvessels, which reside deep below the surface of the brain.

There are several forms of vascular dysfunction that can contribute to the onset of blood flow disturbances and neurodegeneration^{8,9}. One form is a vascular leak that leads to extravasation of serum proteins into the cerebral space and brain antigens into the peripheral circulation. This can occur as a result of inflammation that alters the vessel glycocalyx and tight junctions that normally help maintain the blood-brain barrier. Another form of vascular dysfunction occurs when there is a sudden rupture of a vessel; this leads to hemorrhage and rapid spillage of vessel contents into the

brain parenchyma. A third type of vascular dysfunction is caused by vessel occlusion, which leads to ischemia.

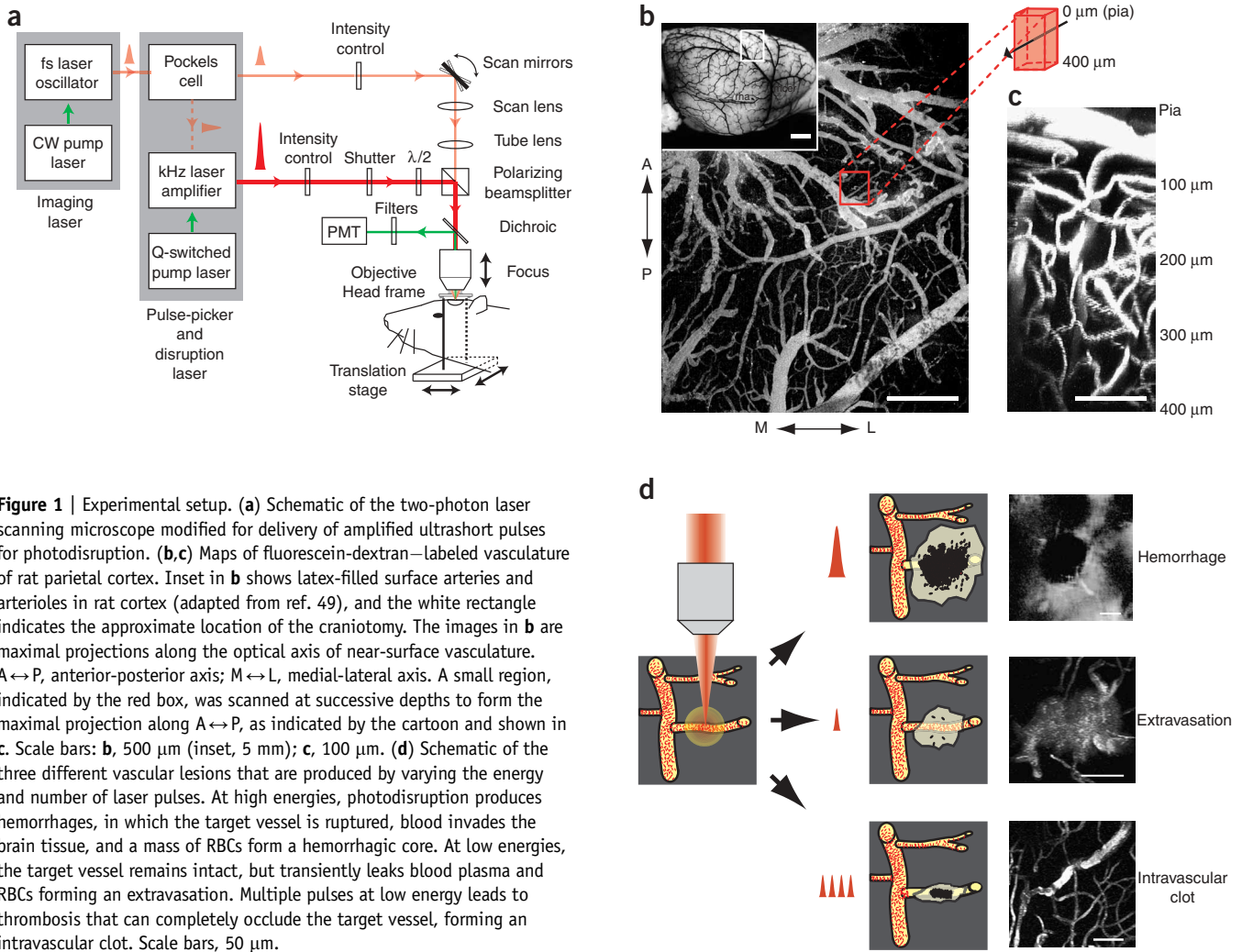
As a means to perturb microvessels in the parenchyma without affecting the surrounding area, we introduce *in vivo* photodisruption of a targeted, deep-lying vessel. Our approach is motivated by past studies^{10,11} that used photothrombotic methods and shaped by recent developments in the nonlinear interaction of light and matter. Nonlinear interactions achieved with high-energy, ultrashort pulses of light at the focus of an objective induce ionization within a femtoliter-sized volume, which leads to the spatially limited release of mechanical energy¹². This suggests the utility of ultrashort laser pulses to directly disrupt vascular cells deep below the cortical surface with minimal collateral damage. A second motivation is the natural integration of photodisruption by high-energy laser light and the imaging of fluorescently labeled tissue at low energy by two-photon laser scanning microscopy (TPLSM)^{13,14} as a means to map the topology and speed of blood flow in surrounding vessels. This combination allows the targeting and real-time monitoring of the photodisruption of individual blood vessels.

RESULTS

Mapping and target selection

Our preparation was the adult rat with an observation window placed over parietal cortex. The underlying vasculature was imaged with *in vivo* TPLSM (**Fig. 1a**), which relies on contrast generated by labeling of the blood plasma with high-molecular-weight fluorescein-dextran. We first mapped vessels throughout the cranial window at low magnification. We acquired planar images of the fluorescent intensity at successive depths in the cortex, which were transformed into maximal projections. We combined projections from several neighboring regions to form a single map of an area of the exposed brain (**Fig. 1b**). We selected target vessels for photodisruption using the criteria that a portion of the vessel coursed parallel to the cortical surface. The vessels comprised parenchymal arterioles, venules and capillaries, with diameters from 5 to 25 μm and subsurface depths of 30 to 480 μm . We identified capillaries by their small diameter, that is, 5–7 μm . To aid in the classification of larger target vessels as arteriole or venule, we traced the

¹Department of Physics, ²Center for Theoretical Biological Physics, ³Department of Neurosciences and ⁴Graduate Program in Neurosciences, 9500 Gilman Drive, University of California at San Diego, La Jolla, California 92093, USA. Correspondence should be addressed to D.K. (dk@physics.ucsd.edu).



shortest path from the target to a surface vessel that was identifiable as a vein or artery.

Once a target was selected and classified, we mapped the local vascular architecture in the vicinity of the target vessel with a three-dimensional stack of high-magnification images (Fig. 1c). We further measured the red blood cell (RBC) velocities in the target vessel and neighboring vessels before and after photodisruption with repetitive line scans¹⁴. Alternatively, the speed of RBCs could be ascertained from the planar images by the orientation of streaks formed by the motion of RBCs.

Insult to the targeted vessel was generated by irradiation of the lumen of the vessel with controlled numbers and energies of amplified, ~100-fs duration pulses of laser light. This process was simultaneous with planar imaging and provided real-time feedback on the progress of the photodisruption (Fig. 1a). The first indication of photodisruption was visualized as the accumulation of fluorescein-dextran outside the vessel lumen. This corresponds to extravasation. In general, the incident pulse energy required to initiate extravasation was at least 0.03 μJ, which corresponds to a threshold fluence for damage of ~1 J/cm² at the focus, consistent with published values¹². Deeper vessels and those lying beneath larger blood vessels required relatively higher

incident energies. Changing the focus location from the lumen to the vessel walls did not affect the extravasation; therefore, we minimized the potential effects of laser light on neuronal tissue by focusing into the vessel lumen.

We generated three forms of vascular disruption (Fig. 1d). High laser pulse energies resulted in hemorrhages with ruptured vasculature. At low laser pulse energies, we achieved two types of vascular disruption that left the target vessel intact: extravasations with continued blood flow and clots with complete vessel occlusion.

Vessel rupture

The most drastic of the insults was the rupture of the target vessel, which led to a hemorrhage of blood plasma and RBCs into the parenchyma (Fig. 2). In these cases, irradiation with laser pulse energies that were well in excess of the threshold value for extravasation was immediately followed by an explosive expansion of fluorescently labeled plasma into the extravascular tissue. A spherical 'core' was often distinguishable from an irregularly shaped volume of fluorescent extravasation as early as 1 s after irradiation. Vessels in the core of the hemorrhage appeared to be completely disrupted. In contrast, we observed intact vessels with moving

RBCs within the volume of extravasation that surrounds the core. Lastly, the size of the core rapidly stabilized (Fig. 2b,c) whereas the extravasation in the tissue that surrounds the core continued to expand for tens of seconds.

Across 17 hemorrhaged vessels in 10 rats, we delivered 1–10 pulses in a single train with an energy per pulse that ranged from 0.2 to 1 μJ . The mean value of 0.8 μJ was equivalent to about $30\times$ the threshold level. We found that the initial radius of the hemorrhage core scaled linearly with the pulse energy (Supplementary Note online). The extravasation of fluorescent blood plasma and isolated RBCs extended beyond the core of the hemorrhage and achieved a radius of $90 \pm 40 \mu\text{m}$ (mean \pm s.d.). The final volume of extravasation, $\sim 10^3$ – 10^4 pl, was independent of the diameter of the vessel and the initial RBC speed (Fig. 2d).

Post-mortem sections showed that the inner core is filled with RBCs (Fig. 2e). Scattered RBCs formed an irregularly shaped hemorrhage that extended from the core. Further, nearby vessels appear to be filled with thrombi that breach vessel walls (Fig. 2e,f). Immunostaining with antibodies against MAP2 demonstrated preserved microtubule integrity in neuropil that is contiguous to the hemorrhage and extravasation site (Fig. 2g).

Extravasation

Reduced laser pulse energies allowed fine control of the vascular lesions. Beginning at a low level of energy, if no vascular changes were observed, we repeated the irradiation at the same or increased pulse energy until we observed some extravasation of blood plasma. This led to an insult in which the target vessel leaked blood plasma and often RBCs into the extravascular tissue, but remained intact with uninterrupted blood flow (Fig. 3a). The radius of the initial extravasation of plasma varied from constrained leakage within several micrometers of the vessel lumen (Fig. 3b) to leakage that extended tens of micrometers into the parenchymal tissue. Limited amounts of additional irradiation, in some cases with increased energy, resulted in further increases in the radius of extravasation (Fig. 3b,c). The blood flow within the vessels continued throughout the irradiation and leakage of vessel (Fig. 3c).

The final incident optical energies that we used to induce extravasation were typically 2 – $3\times$ greater than the threshold energy and in the range of 0.1 to 0.5 μJ , and were delivered in trains of 10 to 100 pulses

(12 vessels in 10 rats). The measured RBC speed after extravasation was $60 \pm 20\%$ of the baseline value (5 vessels in 5 rats; we observed an additional case in which the target vessel doubled in RBC speed after extravasation). In all cases, the leakage of plasma from the

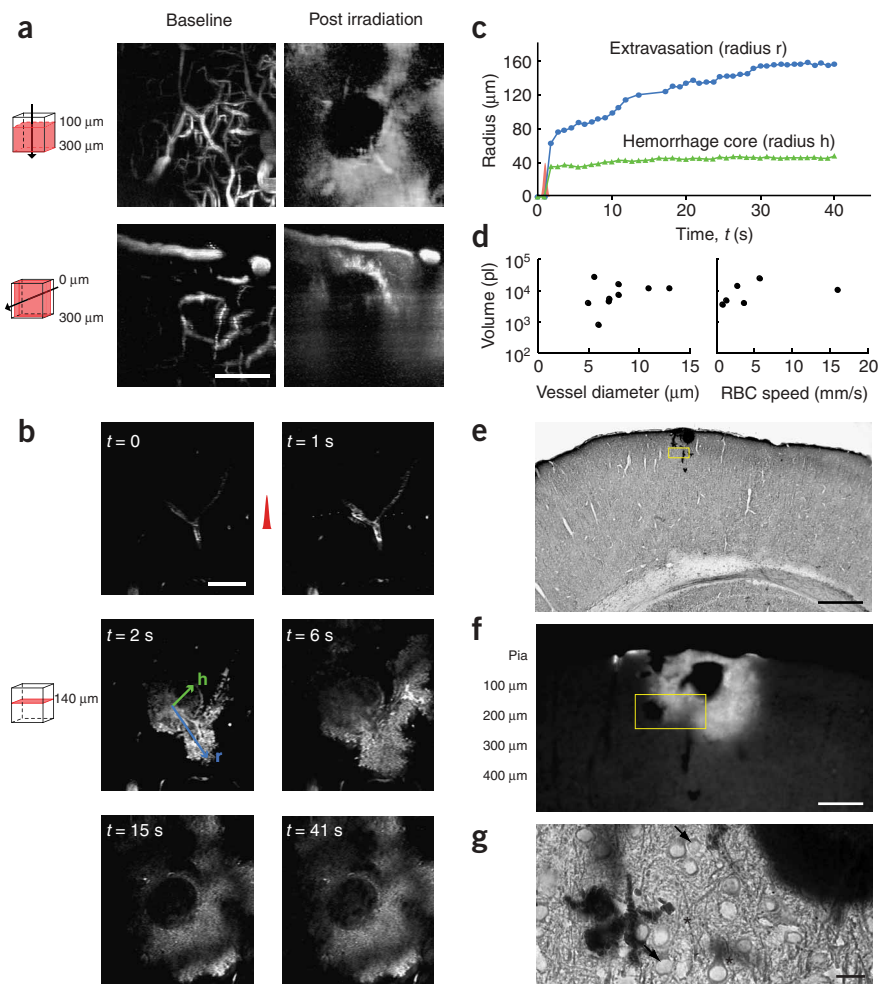
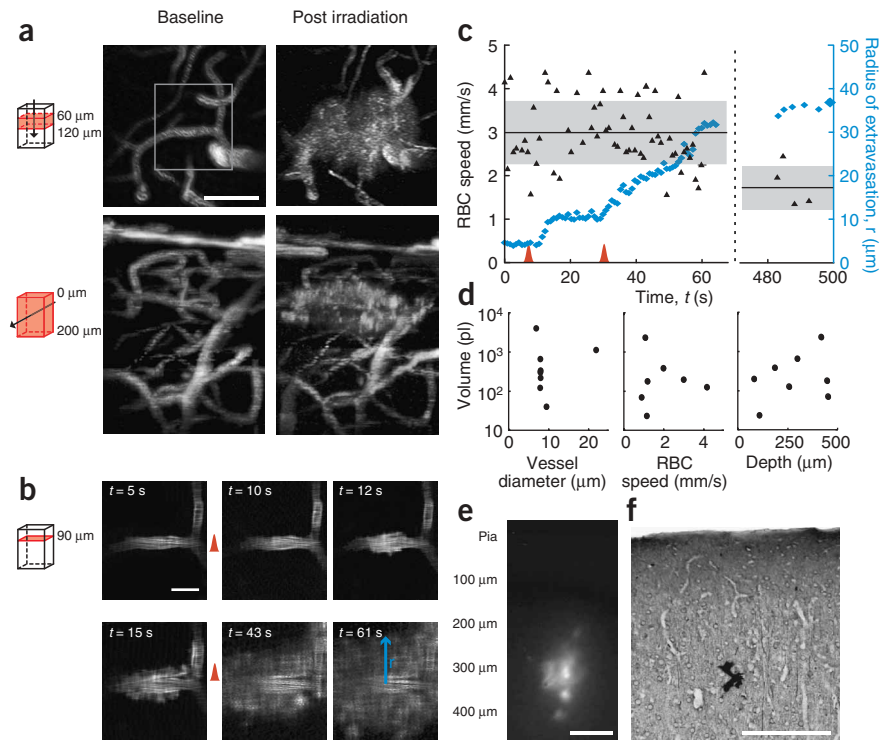


Figure 2 | Hemorrhage via rupture of target vessel. (a) Maximal projections of TPLSM stacks in the vicinity of the target vessel before (left) and after (right) induction of a hemorrhage in a target vessel, 140 μm below cortical surface, by ultrashort laser pulses. After irradiation, the target vessel cannot be seen. Fluorescently labeled blood plasma invades the parenchymal tissue well beyond the extent of the dark spherical volume in the center. Cartoons indicate the directions and volumes of the maximal projections. Scale bar, 100 μm . (b) Temporal sequence of planar images during the formation of the hemorrhage shown in a. The red pulse indicates irradiation with eight 0.6- μJ pulses delivered at 1 kHz. All images were spatially filtered to remove artifacts from pump laser light that leaked through the filters to the PMT, although amplified laser light leaked through and resulted in a series of bright dots in the panel at $t = 1$ s. The arrows marked “r” and “h” indicate the measured radius of the fluorescein-dextran dye and the hemorrhage core, respectively. Scale bar, 50 μm . (c) Graphs of the distance from the center of the targeted vessel to the outer extents of both the core (green) and the extravasated plasma (blue). The red pulse indicates the time of irradiation. Time-zero is matched to that in part b. (d) Volume of extravasated fluorescein versus target-vessel diameter and the initial RBC speed. In both cases, the regression coefficient is statistically insignificant. (e–g) Localization of a hemorrhage in a single coronal tissue section; the rat was killed 40 minutes after the photodisruption of the blood vessel. Panel e shows the diaminobenzidine-stained extravasated RBCs in which the parenchyma was immunolabeled with an antibody against MAP2 (e). Fluorescent imaging of fluorescein-dextran shows that extravasated blood plasma forms a halo that surrounds a central core of the hemorrhage (f). Panel g shows a high-magnification view of the MAP2-labeled section within the box in e and f. Early pathology of somata are highlighted by arrows, and a normal neuronal soma is highlighted by the lower asterisk; immunostaining preserved in a secondary apical dendritic structure is marked by the upper asterisk. Scale bars: e, 500 μm ; f, 100 μm ; g, 20 μm .

Figure 3 | Extravasation of blood constituents into the parenchymal tissue without obstruction of flow in target vessel. **(a)** Maximal projections of TPLSM stacks in the vicinity of the target vessel, located in the center of the field, before (left) and after (right) irradiation with high-energy ultrashort laser pulses. The target vessel was 90 μm below the cortical surface. Note that fluorescein-labeled blood plasma permeates a volume that surrounds the target vessel after irradiation. Cartoons indicate the directions and volumes of the maximal projections. Scale bar, 50 μm . **(b)** Temporal sequence of planar images through the center of the targeted vessel during the formation of the extravasation; the rectangle in **a** shows the location of the field. Streaks visible in the vessel lumens were caused by RBC motion during the image acquisition and indicate blood flow. The arrow marked "r" indicates the measured radius of the extravasation of the fluorescein-dextran dye. Images were spatially filtered to remove artifacts from Q-switched pump laser light leaking through the filters to the PMT. The red pulses denote epochs of irradiation with ~ 500 0.3- μJ laser pulses delivered at 1-kHz. Scale bar, 20 μm . **(c)** Graphs of RBC speed (black triangles; left axis) and radius of extravasation (blue diamonds; right axis) during the irradiation of the target vessel. The red pulses indicate irradiation. The solid line indicates the average speed and the gray band marks the interval of ± 1 s.d. Time-zero is matched to that in part **b**. **(d)** Compilation of the volume of extravasation as a function of the vessel diameter, the initial RBC speed and the depth of the targeted vessel. In all cases the regression coefficient is insignificant. **(e,f)** Photomicrographs of the site of extravasation in a single coronal section imaged with fluorescent illumination **(e)** and bright-field illumination **(f)**; the rat was killed 3 h after the disruption. In **e**, fluorescence of extravasated fluorescein-dextran fills a small area that lies deep to the pial surface. Part **f** illustrates focal accumulation of DAB stained RBCs as well as MAP2-immunostained neurons that are situated in close proximity to the clot. Scale bars: **e**, 100 μm ; **f**, 200 μm .



target vessel stabilized within minutes. The radial distances from the target vessel to the edge of extravasated fluorescein, as judged from planar images, achieved a steady-state value of 40 ± 30 μm . The measured volume of extravasation, $\sim 10^2$ – 10^3 pl, was not correlated with vessel diameter speed, initial RBC speed or with the depth of the vessel (Fig. 3d). We identified *post-mortem* sections from the level of the extravasation by observation of a residual volume of fluorescent labeling in the parenchyma (Fig. 3e). Subsequent staining for RBCs indicated that by the time of death, 3 h after vessel targeting, the extravasation sites were also marked with small aggregates of RBCs (Fig. 3f). Immunostaining with antibodies against MAP2 shows many stained neurons that are contiguous to the center of extravasation. Notably, the volume of tissue superficial to the disrupted vessel was also immunostained, supporting the realization of subsurface targeting.

Intravascular clot
The procedure and laser pulse energies used to produce ischemic clots was an extension of that used to induce extravasation (Fig. 4). After the onset of extravasation, we repeated the irradiation with increased pulse energy and increasing number of pulses until there was a complete cessation of RBC movement in the target vessel (Fig. 4b,c). Immediately after irradiation, the vessel lumen swelled and there was a momentary lack of RBC motion, followed by a restoration of flow. Additional irradiation led to further extravasation, evidenced by the emergence of bright fluorescent patches outside the lumen of the vessel, and ultimately to clot formation,

which was visualized as a nonfluorescent mass within the vessel (Fig. 4b). Measurements of the RBC speed during the photodisruption process showed several transient stops in the flow before a stable clot was formed (Fig. 4c); this clot was observed to remain intact 4 h after irradiation.

We achieved clot formation in 61 microvessels (39 rats) as deep as 480 μm below the surface. In addition, we independently demonstrated clot formation in pial vessels up to 120 μm in diameter, but extensive extravasation from surface vessels made it difficult to visualize vascular dynamics. Across all clots, the final volume of extravasation varied between 10 and 10^4 pl (Fig. 4d), and the volume was independent of the diameter of the vessel, the depth of the vessel and the energy at the focus (Fig. 4e). There was a weak but significant ($P < 0.0001$) increase in volume as a function of the initial RBC speed (Fig. 4e).

We identified the intravascular clot in *post-mortem* tissue sections from aggregates of RBCs (Fig. 5a,b) surrounded by a cloud of extravasated fluorescein-dextran (Fig. 5c). In a representative example ($n = 5$), in which the rat was allowed to survive for 3 h after induction of the clot, immunostaining of MAP2 was present in the neuropil adjacent to the aggregates. The neuronal somata had a range of pathology from cells that appear normal to cells with angulation of cell bodies, an indication of early neuronal pathology (Fig. 5d). As MAP2 immunostaining can be dynamically down-regulated within 1 h of ischemia after large vessel occlusion¹⁵, it is notable that this had not obviously occurred within a 3-h survival time (Fig. 5a) after clot formation.

A histological examination for vascular pathology focused on the region containing the clotted vessel. Anti-fibrin immunoreactivity, a known marker for clotting activity, could be observed in targeted vessels. For the vessel imaged in **Figure 5e**, the fibrin formed a dense core deposit with a more diffuse surround (**Fig. 5f**). This immunostaining was highly overlapped with the extravasated fluorescein in this section (**Fig. 5g**). The dense fibrin core appears associated with a vessel (**Fig. 5h,i**) whose size, orientation and position are consistent with the *in vivo* site of the clotted vessel (**Fig. 5e**). To assay potential damage to perivascular elements, we immunostained for the astrocyte protein vimentin, as this protein is strongly upregulated in reactive astrocytes that proliferate in response to injury¹⁶. Vimentin appeared evenly distributed across the cortex with no increase in staining among the vessels adjacent to the clot (**Fig. 5j,k**).

Finally, we assessed acute ischemic effects across cell types with the hypoxia marker pimonidazole hydrochloride (Hypoxyprobe); this probe labels viable but oxidatively stressed tissue¹⁷. Hypoxyprobe staining was increased in the limited region of fluorescein-dextran extravasation near the clot (**Fig. 5l,m**). Together, these data indicate that clot formation results in a restricted zone of neural pathology (6 clots across 5 rats).

Selectivity of vascular insult

The above definitions of vascular insults offer a convenient categorization scheme, but the observed effects encompass a continuum of effects. Hemorrhages could always be attained at high laser energies (**Fig. 2**). The disruption obtained at low energies (85 vessels) was variable. In eight of the vessels, the initial response was extravasation that rapidly evolved into a clot in the absence of additional pulses, whereas in ten of the vessels the initial response was an unplanned hemorrhage. We achieved stable extravasation in the remaining 67 vessels. In the absence of subsequent laser pulses, we observed flow for at least several minutes (14 vessels; **Fig. 3**). With additional irradiation, a clot formed that completely stopped RBC motion (53 vessels; **Fig. 4**). Although our method does not guarantee the choice of vascular insult, the real-time monitoring of the vasculature with TPLSM assures that the investigator will be able to fully characterize the actual insult.

Blood flow dynamics after a single intravascular clot

To demonstrate the new capabilities of our methodology, we investigated the changes in RBC flow in subsurface vascular

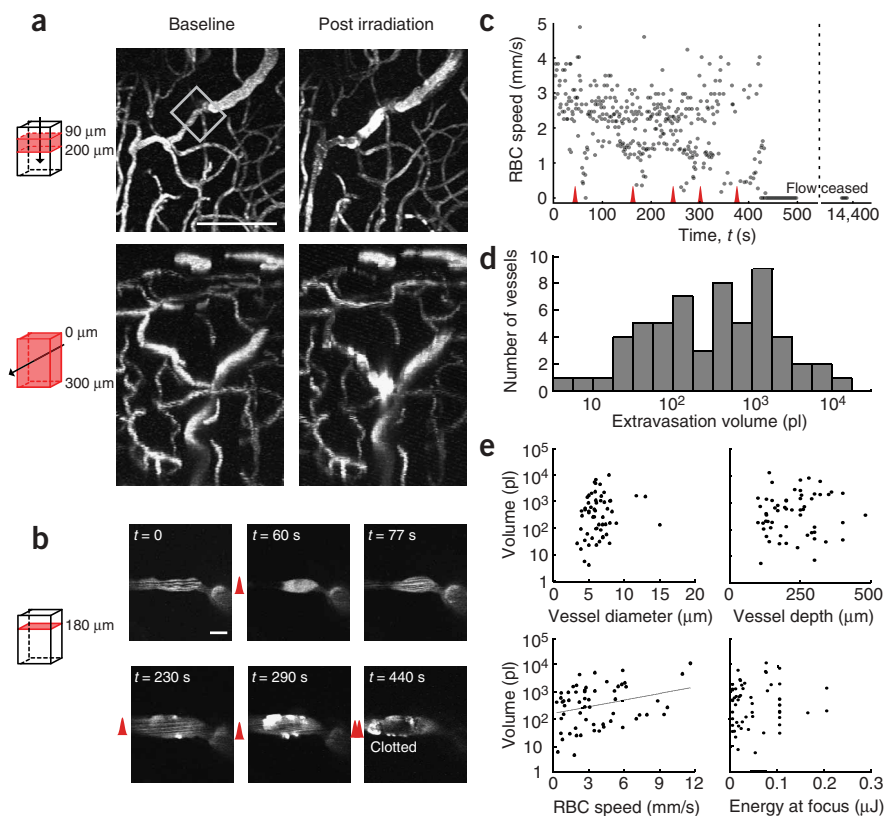
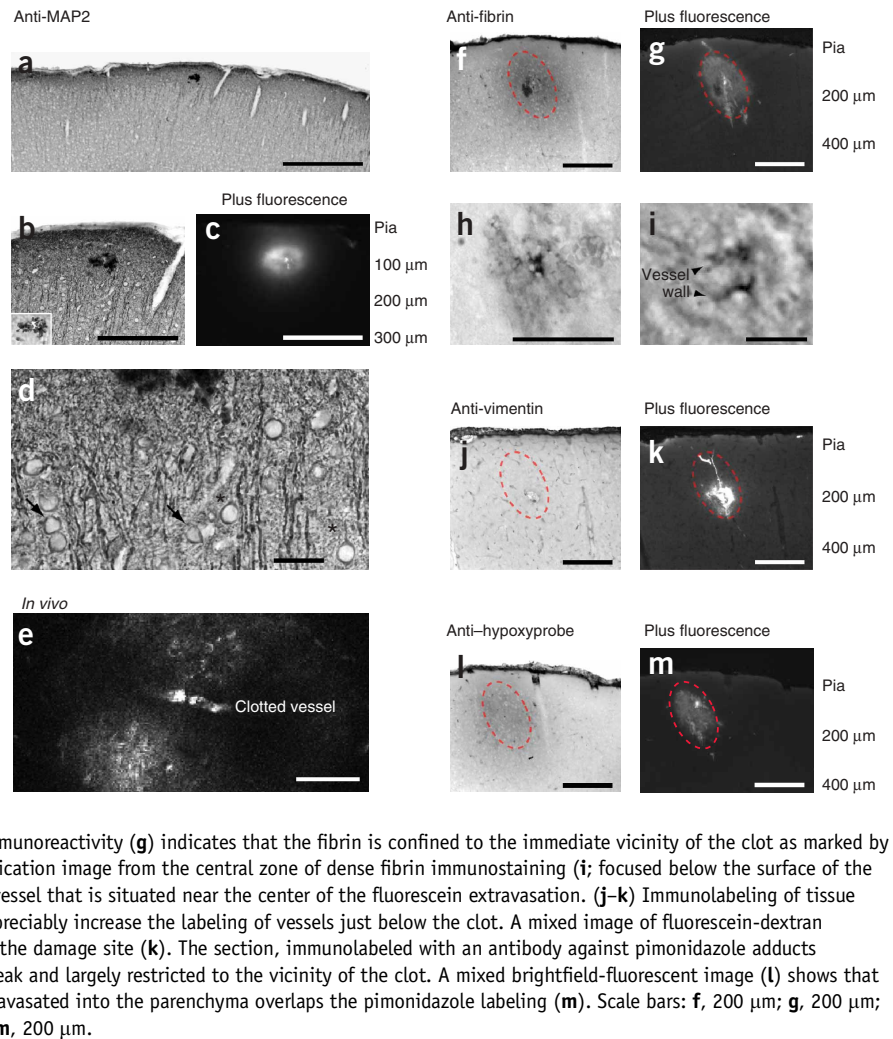


Figure 4 | Intravascular clot in intact target arteriole. **(a)** Maximal projections of TPLSM stacks in the vicinity of the target vessel before (left) and after (right) induction of an ischemic clot in the target vessel, 180 μm below the pial surface, by ultrashort laser pulses. The clot formation was accompanied by some extravasation. Cartoons indicate the directions and volumes of the maximal projections. Scale bar, 100 μm . **(b)** Temporal sequence of planar images during the formation of the intravascular clot; the rectangle in **a** shows the location of the field. The red pulses indicate irradiation with multiple trains of 0.03- μJ pulses delivered at 1 kHz. At $t = 60$ s, there was temporary cessation of RBC motion and swelling of the target vessel immediately after irradiation with two pulses. Flow resumed, as seen at $t = 77$ s. The vessel was then irradiated with five sets of two pulses, which led to limited extravasation ($t = 230$ s). Further irradiation with five 50-pulse trains caused further extravasation ($t = 290$ s). Final irradiation with five 10-pulse trains and five 100-pulse trains led to clot formation and the stable cessation of RBC motion ($t = 440$ s). All images were spatially filtered to remove artifacts from pump laser light that leaked through the filters to the PMT. Scale bar, 10 μm . **(c)** Graph of RBC speed during the formation of a clot in the target vessel. Red pulses indicate irradiation with trains of laser pulses. Time-zero is matched to that in **b**. **(d)** Histogram of the extravasation volumes, measured from the depth of the target vessel up to the surface and then doubled. **(e)** Compilation of the volume of extravasation measured as a function of the vessel diameter, the initial RBC speed, the depth of the targeted vessel and estimated laser pulse energy at the focus. The volume versus speed is fit with the function $\text{Volume/picoliter} = 85 \exp(\text{speed}/(5.2 \text{ mm/s}))$, for which $r = 0.5$ with $P < 0.0001$.

networks that occurred after clot induction. The target vessels consisted of both fine arterioles, 7–9 μm in diameter (6 of 8 rats), and capillaries, ~ 5 μm in diameter (2 of 8 rats). The arterioles were 1 to 2 branches downstream from diving arterioles, as identified by their connectivity with surface arteries, and the capillaries were at least 4 branches away from surface arteries. Data from three examples are shown in **Figure 6a–c**. Before photodisruption, we measured the direction and speed of baseline RBC flow in vessels contiguous to the target vessel (X) to construct vessel-by-vessel flow maps, and we repeated these measurements immediately after a stable clot formed in the target vessel (**Fig. 6a–c**). In all cases, the

Figure 5 | Histological characterization of intravascular clots. (a–d) Localization of a clot in a single coronal tissue section; the rat was killed 3 h after the disruption. DAB-stained RBCs aggregated in the vicinity of the targeted subsurface vessel in a section immunolabeled with an antibody against MAP2 (a and b). Inset in b, a photomicrograph in the plane of the aggregate. Fluorescence imaging of the same area in b shows that the clot is also a site of extravasated fluorescein-dextran (c). High-magnification view just below the clot (d). Immunoreactivity shows minor, early pathology (arrows to angulated neurons) as well as predominantly normal somata (asterisks). Scale bars: a, 500 μm ; b, 200 μm ; c, 200 μm ; d, 20 μm . (e) *In vivo* image, obtained with TPLSM of the clotted microvessel in a view tangential to the surface. The vessel is 250 μm deep to the pial surface. Scale bar, 50 μm . (f–m) Subsequent immunolabeling of tissue from this rat involved pretreatment with peroxide to eliminate staining of endogenous RBCs. A dark reaction product is indicative of immunostained reaction product. The red ellipses delineate a common area in the vicinity of this clot. Anti-fibrin immunostaining indicates localization of fibrin/fibrinogen clot markers (f), which appears as a mixed diffuse zone from extravasated serum that surrounds a small dense region of intense staining. The latter region is shown at higher magnification in h and i. A mixed image of fluorescein-dextran vascular retention and the fibrin immunoreactivity (g) indicates that the fibrin is confined to the immediate vicinity of the clot as marked by the territory of extravasated fluorescein. A high-magnification image from the central zone of dense fibrin immunostaining (i; focused below the surface of the tissue) shows that dense labeling is associated with a vessel that is situated near the center of the fluorescein extravasation. (j–k) Immunolabeling of tissue with the reactive astrocyte marker vimentin did not appreciably increase the labeling of vessels just below the clot. A mixed image of fluorescein-dextran retention and the vimentin immunoreactivity indicates the damage site (k). The section, immunolabeled with an antibody against pimonidazole adducts (Hypoxyprobe), shows that localization of adducts is weak and largely restricted to the vicinity of the clot. A mixed brightfield-fluorescent image (l) shows that the fluorescein-dextran retained in the vessels and extravasated into the parenchyma overlaps the pimonidazole labeling (m). Scale bars: f, 200 μm ; g, 200 μm ; h, 50 μm ; i, 10 μm ; j, 200 μm ; k, 200 μm ; l, 200 μm ; m, 200 μm .



direction of flow in the upstream and parallel vessels was unchanged by the clot, and the magnitude of baseline and post-clot velocities were similar. In contrast, flow in the downstream vessels was often reversed in direction and substantially reduced in magnitude.

We compiled the RBC speeds across all cases. We categorized the vessels we observed by their relation to the target, that is, vessels that lay upstream (U), parallel (P), one and two branches downstream (D1 and D2), and three and four branches downstream (D3 to D4) of the target vessel (Fig. 6d). In upstream and parallel vessels, the preservation of post-clot RBC speed was demonstrated by a distribution of values close to 100% of the baseline value (Fig. 6e). In contrast, the mean post-clot RBC speeds in primary and secondary downstream vessels decreased in magnitude to 7% (0–5% across the lowest three quartiles) and 20% (0–17%) of their respective baseline values (Fig. 6f). The mean post-clot RBC speeds in vessels three and four branches downstream were indistinguishable and reduced to 45% (0–67%) of the baseline value (Fig. 6g). In general, the decrement in RBC speed in downstream vessels encompassed vessels well outside the extent of extravasation around the target vessel. Notably, flow in contiguous vessels that were not supplied by the target were largely unaffected by the occlusion (Fig. 6b).

Restoration of flow after a clot

The localized nature and stability of the subsurface ischemic blockages allowed us to assess possible reperfusion that results from a clinically motivated treatment. We considered two complementary approaches. The first makes use of hypervolumetric hemodilution¹⁸ as a means to reduce the hematocrit and thus the viscosity of the blood. The second makes use of agents that can dissolve clots in otherwise normal vessels^{19,20}.

After clot formation and a reduction in the downstream flow of RBCs (Figs. 4 and 6), we diluted the blood through the injection of isotonic saline during ~30 min. We observed a partial restoration of the flow downstream from the occluded vessel (Fig. 7a). Across a population (8 rats and 55 vessels), those vessels that lay immediately downstream of the occlusion, D1, slowed to less than 10% of baseline speed during the occlusion and were essentially unaffected by hemodilution (Fig. 7b,c). In marked contrast, the flow in vessels that lay one additional branch point away from the occlusion, D2, slowed to approximately 20% of the baseline speed during the occlusion yet almost completely recovered subsequent to hemodilution (Fig. 7b,c). Flow in the D3 and D4 branches was only mildly reduced by the clots (Fig. 6g), although flow was partially restored by hemodilution for these cases as well (Fig. 7b,c).

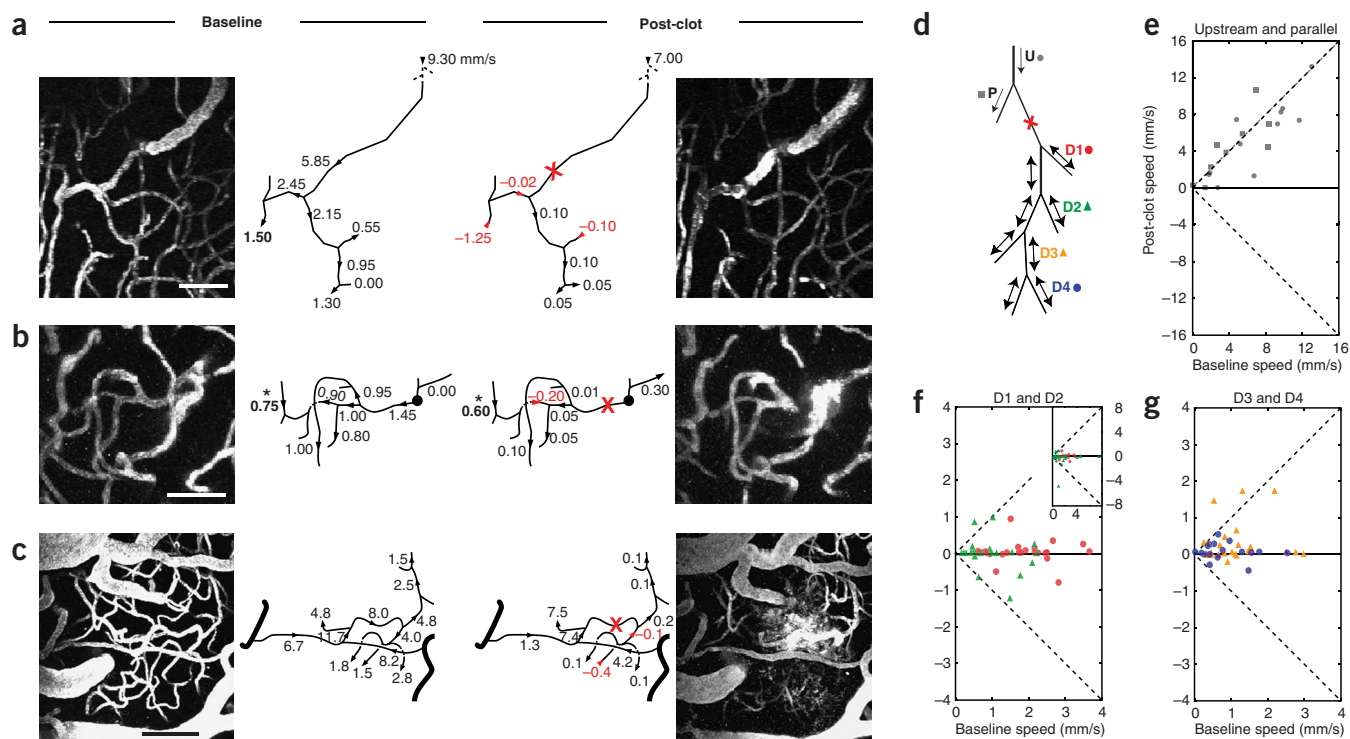


Figure 6 | Changes in RBC velocity around subsurface intravascular clots. (**a–c**) Maximal projections of images of blood flow around intravascular clots before and after clot formation. The schematics indicate RBC velocity in vasculature before and after clot formation. The location of the clot in a targeted vessel is marked by the red X. Negative numbers in red indicate vessels in which the flow direction reversed after clot formation. Projections and schematic of flow, taken 90 to 200 μm below cortical surface, in the vicinity of a targeted arteriole (**a**). The asterisk indicates a downstream vessel whose flow was reversed by the clot but remains high. Projections and schematic of flow in an arteriole that branches off of a diving arteriole, marked by black disc in the schematic, taken through cortex 300 to 400 μm below the pial (**b**). Note that the vessel farthest on the right shows stalled RBCs before the clot, then flowing RBCs after the clot. Although this vessel is near the targeted vessel, it was not clotted by the laser irradiation of the neighboring vessel. The asterisk indicates a vessel whose flow was essentially unaffected by the clot. Projections and schematic of flow, taken through the top 250 μm of cortex, in the vicinity of a targeted arteriole (**c**). The associated capillary network was fed by two surface arterioles that are indicated by the thick lines. Scale bars: **a**, 50 μm ; **b**, 50 μm ; **c**, 100 μm . (**d–g**) Compilation of RBC speeds in vessels connected with a clotted vessel before and after clot formation (132 vessels in 20 networks). The reported speed for each vessel was an average over 37 s. Different symbols indicate the measured vessel's connectivity relative to the clotted vessel (**d**). Standard error of the mean of the measurements are approximately the size of a symbol in the graph. The diagonal lines indicate equal post-clot and baseline magnitudes. The insert for D1 and D2 branches shows a larger dynamic range.

We checked if hemodilution *per se* could substantially increase flow irrespective of the initial clot. The result of control experiments shows that the flow of RBCs in neighboring blood vessels that maintained a separate source from the occluded vessel were essentially unaffected by the clot. The flow in these vessels, located 0.3–1 mm away from the occluded vessel, showed a slight but statistically insignificant increase in speed after hemodilution (Fig. 7c,d).

In the second approach to increase flow after a clot, we attempted to dissolve the clot with recombinant tissue-type plasminogen activator (r-tPA). In 10 rats, we infused r-tPA into the blood after single vessel occlusion (12 occlusions). Peripheral bleeding indicated successful injection, and we confirmed successful r-tPA injection by the immunohistological labeling for r-tPA in sections of brain tissue in the vicinity of the clot (5 of 5 rats). In all cases the vessels remained occluded after r-tPA injections (data not shown). Lastly, we performed three experiments in which we clotted vessels before (4 vessels) and after (8 vessels) the injection of heparin. Heparin did not affect the existing clots or prevent the formation of clots (data not shown).

DISCUSSION

We have demonstrated a method that uses ultrashort pulses of near-infrared laser light for the production of injury to single parenchymal microvessels within the superficial layers of rat cortex while preserving the overlying vasculature. As an application of the intracellular clot model—one of three forms of vascular insult introduced in this work—we evaluated two clinical therapies used for major stroke. Clinical trials have demonstrated occlusions in humans that are unresponsive to thrombolytic therapy, of which r-tPA is a commonly used agent^{19,21}. Similarly, occlusions generated with our technology do not respond to treatment with r-tPA. The manipulation of flow by hemodilution, to decrease the apparent viscosity of the blood²², has been shown to be of clinical use as a treatment for large-scale strokes¹⁸. Our results suggest that such strategies may be an effective means to increase flow around small vessel occlusions.

The high connectivity in brain vascular networks could aid in providing a 'fail-safe' mechanism to maintain flow after blockages^{3,23}. Recent data show that this conjecture is borne out in the network of surface arterioles, in which only a small decrease

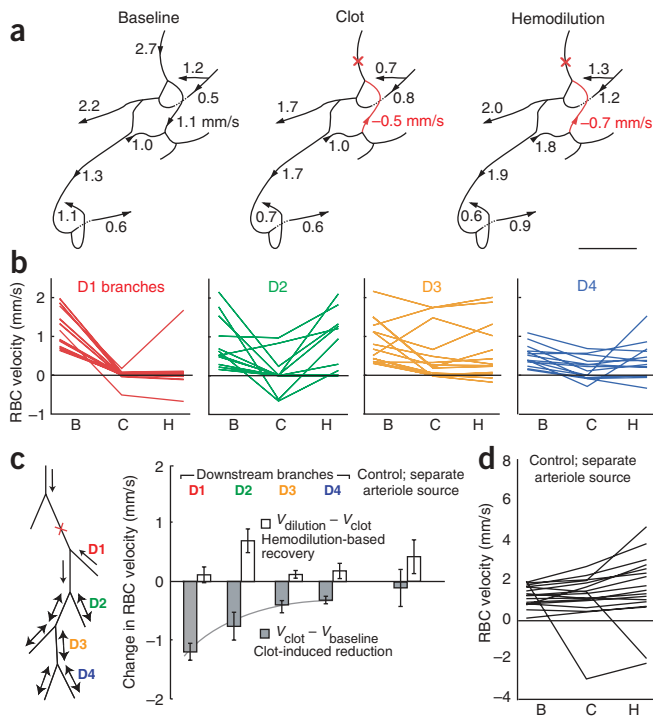


Figure 7 | Changes in RBC velocity around an intravascular clot with hemodilution. The velocities of RBCs were measured before and after clot formation and after hemodilution by intravenous saline. **(a)** RBC velocities at baseline, after occlusion, and after hemodilution in an example network. Red X marks the occluded vessel and vessels in which blood flow reversed direction after occlusion are indicated in red. Scale bar, 50 μm . **(b)** Compilation of RBC speeds in classes of vessels that lie downstream from an occluded vessel before clot formation (baseline), after photoinduced occlusion (clot) and after hemodilution (dilution). Negative velocities indicate that the flow reversed in direction relative to baseline. **(c)** Bar graph showing the differences in RBC velocity before and after hemodilution, *i.e.*, $v_{\text{clot}} - v_{\text{baseline}}$ (gray) and $v_{\text{dilution}} - v_{\text{clot}}$ (white), respectively; error bars, s.e.m. **(d)** Compilation of RBC speeds in control vessels with similar size and speed as noncontrol vessels but which were fed by a different diving arteriole. These vessels were 300 μm to 1 mm away from the target vessel. B, baseline; C, clot; H, hemodilution.

in blood flow is observed downstream from a clotted vessel²⁴. In contrast, we studied deep-lying microvascular networks and found a substantial decrease in RBC speed in vessels downstream from an intravascular clot. The severe drop in blood flow immediately downstream of the clot could reflect distal effects of pathology associated with the clot, such as inflammatory or electrically mediated microvessel constriction. Although we cannot rule out these mechanisms, the persistent nature of flow during extravasation (**Fig. 3c**) suggests that the changes in blood flow subsequent to vessel occlusion are caused largely by the localized clot. This suggests that the reduction in downstream flow after a clot is a consequence of the topology of the subsurface vascular network and the fluid mechanics of blood flow. Support for this interpretation comes from the dramatic reperfusion that occurs in secondary vessels upon hemodilution (**Fig. 7d**). Independent of mechanism, a 90% drop in cortical blood flow that is induced by blockage of a large artery, even for a short duration, is sufficient to cause neurological damage^{25–27}. Thus our data suggest that clots in a

single microvessel could lead to small localized lesions in the brain, such as lacunes²⁸, and that hemodilution may be a means to restrict the extent of this lesion.

Mechanism for vascular damage

Past work has shown that the mechanical disturbance that is induced by nonlinear absorption of ultrashort pulses consists of a cavitation bubble and a shock wave. The size and strength of these disturbances depend on the laser energy absorbed by the tissue¹². Notably, the spherical shape of the hemorrhagic core that results from vessel rupture is consistent with such a mechanism (**Supplementary Note**). For the cases of extravasation and clot formation, which occur at energies close to the damage threshold, the cavitation bubble and shock wave are hypothesized to be too weak to cause vessel rupture, but sufficient to stress endothelial cells and the basement membrane, and trigger the endogenous clotting cascade.

Relation to other neurovascular disease models

The present study complements past work that focused on large ischemic and hemorrhagic disruptions, which helped to define the molecular basis for neurovascular pathology. This includes the induction of failures in the blood-brain barrier by the injection of agents that weaken vessels or disrupt the blood-brain barrier^{29–31}. A prior approach to model hemorrhages made use of the injection of blood or blood constituents directly into the parenchyma³². This has the advantage of good spatial localization, yet the volume of the hemorrhage is relatively large. Our induction of blood extravasation may provide a unique means to model microbleeds, that is, localized, small hemorrhages observed in aged human patients³³.

Occlusion of large surface vessels has been variously modeled via the surgical insertion of a filament^{34,35}, ligation³⁶ or the optical irradiation of large surface vessels in conjunction with a blood-born photosensitizer^{37,38}. Existing models of small ischemic strokes involve the intravascular injection of small clotting agents, such as microspheres³⁹ or pre-formed emboli⁴⁰, or the *in situ* formation of emboli⁴¹. Such models have been of proven use for preclinical efficacy studies of therapeutic agents, yet are a challenge for real-time studies as the locations and extent of the occlusions can be variable. Our methodology obviates many of these difficulties and provides a useful tool to perturb and measure neurovascular coupling, a long-standing challenge in stroke research⁴².

METHODS

Surgical preparation. Our subjects were 55 male Sprague-Dawley rats, 100–350 g in mass, that were anesthetized by interperitoneal injection of urethane (150 mg per 100 g rat), supplemented as necessary. We delivered atropine sulfate by subcutaneous injection (5 μg per 100 g rat) at the start of surgery and supplemented hourly (1 μg per 100 g rat). We also added 5% (wt/vol) glucose in physiological saline (0.5 ml per 100 g rat) every hour. We maintained rat body temperature at 37.5 $^{\circ}\text{C}$ with a heating blanket (model 507053; Harvard), and blood oxygen levels and heart rate were monitored in a subset of rats with a pulse oxymeter (model 8600V; Nonin). We prepared a 4 \times 6 mm craniotomy over the parietal cortex. We removed the dura, glued a chamber consisting of a metal frame and a removable glass coverslip (no. 1) lid to the skull, and filled the space between the exposed brain surface and the coverglass with 1.5% (wt/vol) agarose (Sigma) in an artificial

cerebro-spinal fluid⁴³. To visualize the vasculature and the motion of RBCs with TPLSM, we injected ~0.3 ml of a 5% (wt/vol) solution of 2 MDa fluorescein-conjugated dextran (FD-2000S; Sigma) in physiological saline intravenously. The care and experimental manipulation of our animals have been reviewed and approved by the Institutional Animal Care and Use Committee at the University of California, San Diego.

Two-photon laser scanning microscopy. Images were obtained with a two-photon laser scanning microscope of local design⁴⁴, which was modified to include an amplified beam (Fig. 1a)⁴⁵. Low-energy, 100-fs, 76-MHz pulses for TPLSM were generated by a Titanium:Sapphire laser oscillator (Mira F-900; Coherent Inc.) that was pumped by a continuous wave (CW) laser (Verdi V-10 Nd:YVO₄ laser; Coherent Inc.). The imaging laser pulses were scanned in a raster pattern by galvanometric mirrors that are relay-imaged to the back aperture of the objective. The two photon-excited fluorescence is reflected by a dichroic mirror and relayed to a photomultiplier tube (PMT). To produce laser pulses for photodisruption, we used a Pockels cell (QS-3 with NVP-525D driver and DD1 timing circuit; Quantum Technologies) to reroute 1 in 76,000 pulses from the oscillator pulse train to seed a multipass Titanium:Sapphire amplifier that is pumped by a Q-switched laser (Corona; Coherent). A half-wave plate ($\lambda/2$) rotates the polarization of the amplified pulses to lie perpendicular to that of the laser oscillator and thus allows both the photodisruption beam and the imaging beam to be routed to the microscope objective with a polarizing beamsplitter. We used a 0.12 numerical aperture (NA), 5 \times -magnification air objective (Olympus) to obtain images of the surface vasculature across the entire cranial window to aid in navigating around the cortical vasculature. We changed to a 0.8-NA, 40 \times , water-immersion objective (Olympus) for high-resolution imaging, line-scan measurements and photodisruption. The energy per pulse of the imaging beam never exceeded an incident value of 1 nJ on cortex.

We obtained individual planar images that spanned the area surrounding the target vessel, or sets of images at 1- μ m axial spacing, both before and after photodisruption. We also used planar images to monitor the production of the vascular disruptions in real time. We used line scans along single vessels, with a maximum scan rate of 1.3 kHz, to quantify RBC velocity¹⁴. In some cases, we extracted information about RBC velocity from frames of images in which the fast-scanning axis of the imaging beam was aligned with the vessel axis and the distance between successive scans along the slow-scanning axis was small compared to the size of an RBC. Here, the motion of RBCs results in diagonal streaks in the image and the slope of the streak is inversely proportional to the RBC velocity.

Photodisruption. Photodisruption of microvasculature made use of high-energy pulses that were generated with a multi-pass Ti:Al₂O₃ amplifier of local construction that followed a previously published design⁴⁶ and operated at a 1 kHz pulse-rate. The photodisruption beam and the imaging beam were combined before the microscope objective with a polarizing beamsplitter (Fig. 1a). We focused the two beams in the same focal plane and centered the amplified beam in the area that is raster-scanned by the imaging beams so that photodisruption occurred at the center of the TPLSM imaged field. The energy per pulse of the photo-

disruption beam was varied with neutral density filters and the number of pulses was controlled by a mechanical shutter (Uniblitz LS3Z2 shutter and VMM-D1 driver; Vincent). The energy and number of pulses was modified based on damage assessed from the real-time TPLSM images.

Hemodilution. We achieved a drop in hematocrit by the uniform injection of 35 ml of saline per kg rat, that is, one-half of the estimated blood volume, into the tail vein or the femoral vein over a period of 30 min. This results in a reduction in hematocrit to 90% of the baseline value (3 rats), as assayed by packed cell volume, at the end of 30 min.

Anticoagulants. In a selected group of rats, we injected r-tPA (Genentech) via the tail vein (4 rats) or via the carotid artery (6 rats) after we observed the clots to be stable for 30 min. The rate of injection was 10 mg per kg rat per hour and was continued until the r-tPA caused bleeding to appear at the cranial window. The final dosage varied between 6.3 and 23 mg per kg rat with an average 13 mg per kg rat. This dosage is higher than the typical dose of 5 to 10 mg per kg rat administered to break clots in the middle cerebral artery^{47,48}. Heparin (Elkiins-Sinn) was injected intravenously at 100 units per rat.

Additional methods. Our methods for the estimation of extravasation volume and *post-mortem* analysis, which includes Hypoxyprobe-1 labeling and immunohistochemistry, are described in **Supplementary Methods** online.

Note: Supplementary information is available on the Nature Methods website.

ACKNOWLEDGMENTS

We thank Q. Cheng for assistance with the plasminogen activator experiments, E. Dolnick for assistance with the electronics, D. Pizzo and L. Thal for use of their photomicroscope, L. Schroeder and S. Siegel for discussions, and Coherent, Inc. for the loan of equipment. This work was funded by the David and Lucille Packard Foundation, the National Science Foundation (DBI/0455027), the National Institutes of Health (NS/041096, NS/043300, EB/003832 and RR/021907), a La Jolla Interfaces in Science Postdoctoral Fellowship to C.B.S. and a National Science Foundation Graduate Fellowship to N.N.

COMPETING INTERESTS STATEMENT

The authors declare that they have no competing financial interests.

Published online at <http://www.nature.com/naturemethods/>
Reprints and permissions information is available online at
<http://npg.nature.com/reprintsandpermissions/>

- Hudetz, A.G. Percolation phenomenon: The effect of capillary network rarefaction. *Microvasc. Res.* **45**, 1–10 (1993).
- Moody, D.M., Bell, M.A. & Challa, V.R. Features of the cerebral vascular pattern that predict vulnerability to perfusion or oxygenation deficiency: An anatomic study. *AJNR Am. J. Neuroradiol.* **11**, 431–439 (1990).
- Brozici, M., van der Zwain, A. & Hillen, B. Anatomy and functionality of leptomeningeal anastomoses: A review. *Stroke* **34**, 2750–2762 (2003).
- Cox, S.B., Woolsey, T.A. & Rovainen, C.M. Localized dynamic changes in cortical blood flow with whisker stimulation corresponds to matched vascular and neuronal architecture of rat barrels. *J. Cereb. Blood Flow Metab.* **13**, 899–913 (1993).
- Iadecola, C. Neurovascular regulation in the normal brain and in Alzheimer's disease. *Nat. Rev. Neurosci.* **5**, 347–360 (2004).
- Wardlaw, J.M., Sandercock, P.A., Dennis, M.S. & Starr, J. Is breakdown of the blood-brain barrier responsible for lacunar stroke, leukoaraiosis, and dementia? *Stroke* **34**, 806–812 (2003).
- Cullen, K.M., Zoltan, K. & Stone, J. Pericapillary haem-rich deposits: Evidence for microhaemorrhages in aging human cerebral cortex. *J. Cereb. Blood Flow Metab.* **25**, 1656–1667 (2005).

8. del Zoppo, G.J. Microvascular changes during cerebral ischemia and reperfusion. *Cardiovascular and Brain Metabolism Reviews* **6**, 47–96 (1994).
9. Farkas, E. & Luiten, P.G.M. Cerebral microvascular pathology in aging and Alzheimer's disease. *Prog. Neurobiol.* **64**, 575–611 (2001).
10. Watson, B.D., Dietrich, W.D., Busto, R., Wachtel, M.S. & Ginsberg, M.D. Induction of reproducible brain infarction by photochemically initiated thrombosis. *Ann. Neurol.* **17**, 497–504 (1985).
11. Haseldonckx, M., van Bedaf, D., van de Ven, M., van Reempts, J. & Borgers, M. Vasogenic oedema and brain infarction in an experimental penumbra model. *Acta Neurochir. (Wien)* **76** (Suppl.), 105–109 (2000).
12. Vogel, A. & Venugopalan, V. Mechanisms of pulsed laser ablation of biological tissues. *Chem. Rev.* **103**, 577–644 (2003).
13. Svoboda, K., Denk, W., Kleinfeld, D. & Tank, D.W. *In vivo* dendritic calcium dynamics in neocortical pyramidal neurons. *Nature* **385**, 161–165 (1997).
14. Kleinfeld, D., Mitra, P.P., Helmchen, F. & Denk, W. Fluctuations and stimulus-induced changes in blood flow observed in individual capillaries in layers 2 through 4 of rat neocortex. *Proc. Natl. Acad. Sci. USA* **95**, 15741–15746 (1998).
15. Dawson, D.A. & Hallenbeck, J.M. Acute focal ischemia-induced alterations in MAP2 immunostaining: Description of temporal changes and utilization as a marker for volumetric assessment of acute brain injury. *J. Cereb. Blood Flow Metab.* **16**, 170–174 (1996).
16. Latov, N. *et al.* Fibrillary astrocytes proliferate in response to brain injury. *Dev. Biol.* **72**, 381–384 (1979).
17. Chapman, J.D., Franko, A.J. & Sharplin, J. A marker for hypoxic cells in tumours with potential clinical applicability. *Br. J. Cancer* **43**, 546–550 (1981).
18. Asplund, K. Haemodilution for acute ischaemic stroke (a review). *Cochrane Database Syst. Rev.* **3**, 1–41 (2005).
19. Sakharov, D.V., Barrett-Bergshoeff, M., Hekkenberg, R.T. & Rijken, D.C. Fibrin-specificity of a plasminogen activator affects the efficiency of fibrinolysis and responsiveness to ultrasound: Comparison of nine plasminogen activators *in vitro*. *Thromb. Haemost.* **81**, 605–612 (1999).
20. The GUSTO Angiographic Investigators. The effects of tissue plasminogen activator, streptokinase, or both on coronary-artery patency, ventricular function, and survival after acute myocardial infarction. *N. Engl. J. Med.* **319**, 1615–1622 (1993).
21. Lyden, P.D. *Thrombolytic Stroke Therapy, 2nd Edition* (Humana Press, New Jersey, 2004).
22. Skalak, R., Chen, P.H. & Chien, S. Effect of hematocrit and rouleaux on apparent viscosity in capillaries. *Biorheology* **9**, 67–83 (1972).
23. Goldman, D. & Popel, A.S. A computational study of the effect of capillary network anastomoses and tortuosity on oxygen transport. *J. Theor. Biol.* **206**, 181–194 (2000).
24. Schaffer, C.B. *et al.* Two-photon imaging of cortical surface microvessels reveals a robust redistribution in blood flow after vascular occlusion. *Public Library of Science, Biology*; in the press.
25. Baron, J.C. Perfusion thresholds in human cerebral ischemia: Historical perspective and therapeutic implications. *Cerebrovasc. Dis.* **11**, 2–8 (2001).
26. Hossmann, K.A. Viability thresholds and the penumbra of focal ischemia. *Ann. Neurol.* **36**, 557–565 (1994).
27. Zhao, W., Belayev, L. & Ginsberg, M.D. Transient middle cerebral artery occlusion by intraluminal suture II. Neurological deficits, and pixel-based correlation of histopathology with local blood flow and glucose utilization. *J. Cereb. Blood Flow Metab.* **17**, 1281–1290 (1997).
28. O'Brien, J.T. *et al.* Vascular cognitive impairment. *Lancet Neurol.* **2**, 89–98 (2003).
29. Dobrogowska, D.H., Lossinsky, A.S., Tarnawski, M. & Vorbrodt, A.W. Increased blood-brain barrier permeability and endothelial abnormalities induced by vascular endothelial growth factor. *J. Neurocytol.* **27**, 163–173 (1998).
30. Rosenberg, G.A., Mun-Bryce, S., Wesley, M. & Kornfeld, M. Collagenase-induced intracerebral hemorrhage in rats. *Stroke* **21**, 801–807 (1990).
31. Dijkhuizen, R.M., Asahi, M., Wu, O., Rosen, B.R. & Lo, E.H. Rapid breakdown of microvascular barriers and subsequent hemorrhagic transformation after delayed recombinant tissue plasminogen activator treatment in a rat embolic stroke model. *Stroke* **33**, 2100–2104 (2002).
32. Kaufman, H.H. *et al.* A rabbit model of intracerebral hematoma. *Acta Neuropathol. (Berl.)* **65**, 318–321 (1985).
33. Fazekas, F. *et al.* Histopathologic analysis of foci of signal loss on gradient-echo T2*-weighted MR images in patients with spontaneous intracerebral hemorrhage: Evidence of microangiopathy-related microbleeds. *AJNR Am. J. Neuroradiol.* **20**, 637–642 (1999).
34. Lyden, P.D., Jackson-Friedman, C., Shin, C. & Hassid, S. Synergistic combinatorial stroke therapy: A quantal bioassay of a GABA agonist and a glutamate antagonist. *Exp. Neurol.* **163**, 477–489 (2000).
35. Longa, E.Z., Weinstein, P.R., Carlson, S. & Cummins, R. Reversible middle cerebral artery occlusion without craniectomy in rats. *Stroke* **20**, 84–91 (1989).
36. Wei, L., Rovainen, C.M. & Woolsey, T.A. Ministrokes in rat barrel cortex. *Stroke* **26**, 1459–1462 (1995).
37. Yao, H. *et al.* Photothrombotic middle cerebral artery occlusion and reperfusion laser system in spontaneously hypertensive rats. *Stroke* **34**, 2716–2721 (2003).
38. Nakase, H., Kakizaki, T., Miyamoto, K., Hiramatsu, K. & Sakaki, T. Use of local cerebral blood flow monitoring to predict brain damage after disturbance to the venous circulation: Cortical vein occlusion model by photochemical dye. *Neurosurgery* **37**, 280–285 (1995).
39. Takeo, S., Miyake, K., Minematsu, R., Tanonaka, K. & Konishi, M. *In vitro* effect of naftidrofuryl oxalate on cerebral mitochondria impaired by microsphere-induced embolism in rats. *J. Pharmacol. Exp. Ther.* **248**, 1207–1214 (1989).
40. Kudo, M., Aoyama, A., Ichimori, S. & Fukunaga, N. An animal model of cerebral infarction. Homologous blood clot emboli in rats. *Stroke* **13**, 505–508 (1982).
41. Futrell, N. *et al.* A new model of embolic stroke produced by photochemical injury to the carotid artery in the rat. *Ann. Neurol.* **23**, 251–257 (1988).
42. Lo, E.H., Dalkara, T. & Moskowitz, M.A. Mechanisms, challenges and opportunities in stroke. *Nat. Rev. Neurosci.* **4**, 399–415 (2003).
43. Kleinfeld, D. & Delaney, K.R. Distributed representation of vibrissa movement in the upper layers of somatosensory cortex revealed with voltage sensitive dyes. *J. Comp. Neurol.* **375**, 89–108 (1996).
44. Tsai, P.S. *et al.* Principles, design, and construction of a two photon laser scanning microscope for *in vitro* and *in vivo* brain imaging. In *In Vivo Optical Imaging of Brain Function* (ed. Frostig, R.D. ed.) 113–171 (CRC Press, Boca Raton, 2002).
45. Tsai, P.S. *et al.* All-optical histology using ultrashort laser pulses. *Neuron* **39**, 27–41 (2003).
46. Backus, S. *et al.* High-efficiency, single-stage 7-kHz high-average-power ultrafast laser system. *Opt. Lett.* **26**, 465–467 (2001).
47. Zhang, R.L., Zhang, Z.G. & Chopp, M. Increased therapeutic efficacy with rt-PA and anti-CD18 antibody treatment of stroke in the rat. *Neurology* **15**, 273–279 (1999).
48. Korninger, C. & Collen, D. Studies on the specific fibrinolytic effect of human extrinsic (tissue-type) plasminogen activator in human blood and in various animal species *in vitro*. *Thromb. Haemost.* **46**, 561–565 (1981).
49. Scremin, O.U. Cerebral vascular system. In *The Rat Nervous System* (Paxinos, G. ed.) 3–35 (Academic Press, Inc., San Diego, 1995).